Tribology International 90 (2015) 164–174

Contents lists available at ScienceDirect

Tribology International

journal homepage: www.elsevier.com/locate/triboint

On the boundary conditions in multi-phase flow through the piston ring-cylinder liner conjunction

H. Shahmohamadi [a], M. Mohammadpour [a], R. Rahmani [a], H. Rahnejat [a,*], C.P. Garner [a], S. Howell-Smith [b]

[a] Wolfson School of Mechanical and Manufacturing Engineering, Loughborough University, Loughborough, LE11 3TU Leicestershire, UK
[b] Capricorn Automotive Ltd., Basingstoke, Hampshire, UK

ARTICLE INFO

Article history:
Received 6 November 2014
Received in revised form
25 March 2015
Accepted 16 April 2015
Available online 24 April 2015

Keywords:
Mixed multi-phase regime of lubrication
Zero reverse inlet boundary
Cavitation
Friction

ABSTRACT

Prediction of load capacity and friction depends on the assumed boundary conditions. The inlet comprises swirl and counter flows, admitting only a portion of the inward flow into the conjunctional gap. At the contact exit, the lubricant film ruptures with multi-phase flow through a cavitation region. Therefore, the boundary conditions affect the load carrying capacity and friction. A Navier–Stokes solution of multi-phase flow, including vapour transport is presented, with determined realistic boundary conditions.

The evaluated boundaries agree with potential flow analysis satisfying compatibility conditions, not hitherto reported in literature. The investigation is extended to the determination of optimum compression ring contacting geometry.

1. Introduction

The main function of the compression ring in the piston-ring pack is to seal the combustion chamber. This reduces low-by, lubricant degradation and power loss. Effective sealing prevents the high-pressure gases escaping from the combustion chamber as well as lubricant leakage into it. Therefore, sealing is critical for improved efficiency and reduced emissions. However, ideal sealing yields a diminished ring-cylinder liner conjunctional gap, which worsens friction [1]. Piston assembly accounts for approximately 35–45% of all the internal combustion engine frictional losses [2]. The top compression ring's contribution is nearly 30% of these losses, which translates to 2–3% of the fuel energy consumption. Therefore, it is essential to strike a balance between good sealing function and low friction. To gain a good insight into the interplay between sealing, load carrying capacity and frictional characteristics of the piston ring conjunctional gap, a plethora of issues need to be addressed, making for very complex and time intensive numerical analysis. These issues include physical non-conformity of an elastic ring (subject to modal elastodynamic behaviour: in its radial plane [3] as well as axially out-of-plane such as ring flutter [4]) with the cylinder bore, which in reality is not an idealised right circular cylinder, either radially or in its axial profile [5]. The non-conformity leads to loss of sealing and blow-by as well as oil loss and cavitation in diverging gaps. Most analyses disregard circumferential non-conformity of ring-bore conjunctional gap as this would depend on the engine cylinder configuration. This approach, although idealistic, yields a generic-type solution. It also leads to a one dimensional solution for ring-bore conjunctional gap in the axial direction of the ring (*i.e.* along the ring's contacting face-width profile).

An important consideration is the use of realistic boundary conditions. In most hydrodynamic analyses a fully-flooded (drowned) inlet boundary is assumed, again to keep within a generic approach. However, it is clear, through observation of wear as well as *in situ* measurements of friction using floating liner methods [6–8] that an insufficient supply of lubricant exists in parts of the piston cycle. In the upstroke motion of the piston, the inlet to the top compression ring conjunctional gap resides within the combustion chamber. There would unlikely be a sufficient supply of lubricant in such instances to assume a fully flooded inlet. In fact, it is shown that mixed or boundary regime of lubrication is prevalent at instances of contact reversal by many numerical predictions [9–10] and experimental measurements of friction [6–8]. Therefore, determination of appropriate inlet boundary conditions, leading to contact starvation is essential for realistic prediction of prevailing tribological conditions. The same is also true of contact outlet boundary conditions, where the falling pressures in a diverging gap result in lubricant film rupture in the presence of retarding

* Corresponding author.
E-mail address: h.rahnejat@lboro.ac.uk (H. Rahnejat).

http://dx.doi.org/10.1016/j.triboint.2015.04.025

Nomenclature

A	apparent contact area
A_a	asperity contact area
b	ring axial face-width
c	maximum crown height of ring
d	ring thickness
E_1	Young's modulus of elasticity of the ring
E_2	Young's modulus of elasticity of the liner
E'	equivalent (reduced) modulus of elasticity
f_b	boundary friction
f_{mass}	vapour mass function
f_t	total friction
f_v	viscous friction
F_T	ring tension force
F_G	combustion gas force
F_2, $F_{5/2}$	statistical functions
g	ring end gap
h	elastic film shape
h_s	ring axial profile
I	ring cross-sectional second area moment of inertia
k	speed ratio
l	connecting rod length
L	ring peripheral length
P_f	frictional power loss
p	absolute pressure
p_{atm}	atmospheric pressure
p_{sat}	liquid saturation vaporisation pressure
p_L	ring lower edge pressure
p_U	ring upper edge pressure
p_e	elastic pressure
p_g	gas pressure
p_h	hydrodynamic pressure
r	crank-pin radius
r_0	nominal bore radius
R_c,R_e	transfer source terms related to the growth and collapse of the vapour bubbles
t	time
ΔU	ring sliding velocity
U_1, U_2	surface velocities of contacting bodies
$\vec{V}$	velocity vector
$\vec{V}_v$	velocity vector of the vapour phase
W	contact load
W_a	load share of asperities
W_h	load carried by the lubricant film
x	axial position along ring face width
x_c	oil film rupture point
Z	pressure–viscosity index

Greek symbols

α_0	pressure–viscosity coefficient
β_0	temperature–viscosity coefficient
φ	crank angle
λ	Stribeck's oil film parameter
ζ	number of asperity peaks per unit contact area
η	lubricant dynamic viscosity
η_0	lubricant dynamic viscosity at atmospheric pressure
κ	average asperity tip radius
$\lambda_,$	Stribeck's oil film parameter
λ'	pressure-induced shear coefficient
ϑ_i	ratio of the film thickness at the stagnation point to the central film thickness
ϑ_e	ratio of the film thickness at the rupture point to the central film thickness
ν_1	Poisson's ratio of the ring material
ν_2	Poisson's ratio of the liner material
ρ	lubricant density
ρ_0	lubricant density at atmospheric pressure
ρ_m	mixture density
ρ_v	vapour density
σ_r	liner surface roughness
σ_l	ring surface roughness
σ_{RMS}	root mean square roughness of the counterface: $\sigma_{RMS}=\sigma_r+\sigma_l$
τ	shear stress
τ_L	limiting shear stress
τ_{L0}	limiting shear stress at atmospheric pressure
Γ	diffusion coefficient
ω	engine rotational speed

friction, which also causes cavitation. The effect of cavitation was studied by Chong et al. [11], who used Elrod's approximation [12] to the Jakobsson and Floberg [13] and Olsson [14] (JFO) cavitation boundary conditions. Other general cavitation algorithms, taking into account the effect of lubricant compressibility, arising from conjunctional geometry or surface topography, whilst upholding the conservation of mass flow have also been reported [15]. Chong et al. [11] showed that cavitation reduces the lubricant availability at the Top Dead Centre (TDC) reversal, thus causing a starved contact in parts of the power stroke in the vicinity of the TDC. With the Elrod algorithm, the continuity of Couette flow is only assured, whilst the usually assumed Swift–Stieber outlet boundary condition does not embody the principle of conservation of mass flow. Therefore, in order to accurately determine the position of film rupture at the exit boundary condition, the principle of conservation of mass flow would necessitate the solution of Navier–Stokes equations. This was the approach undertaken by Shahmohamadi et al. [16] who provided a combined solution of Navier–Stokes and energy equations for the ring-bore contact with an assumed fully flooded inlet. No lubricant outlet boundary conditions were imposed. This is the approach also undertaken in the current paper, also taking into account the vapour transport equation and the Rayleigh–Plesset void fraction. Additionally, only pressure boundary conditions are imposed, instead of those based on lubricant availability such as a fully flooded inlet. This expounded approach, not hitherto reported in literature, is more realistic and without artificially imposed lubricant flow conditions. In practice observation of flow at the boundary points has shown some reverse flow, which is dependent upon surface velocities of the contiguous solids as well as thermal conditions. An analytical approach was presented by Tipei [17], based on potential flow, surface velocities and compatability conditions to replicate the observations for the case of rolling contacts. Recently, analysis of rolling circular point contact by Mohammadpour et al. [18] using Tipei's boundary conditions showed very good agreement with the experimental work initially reported by Johns-Rahnejat and Gohar [19]. Therefore, additionally this paper extends the approach of Tipei [17] to the case of sliding contact of compression ring along the cylinder liner to establish the validity of potential flow analysis at boundary points against the full Navier–Stokes solution.

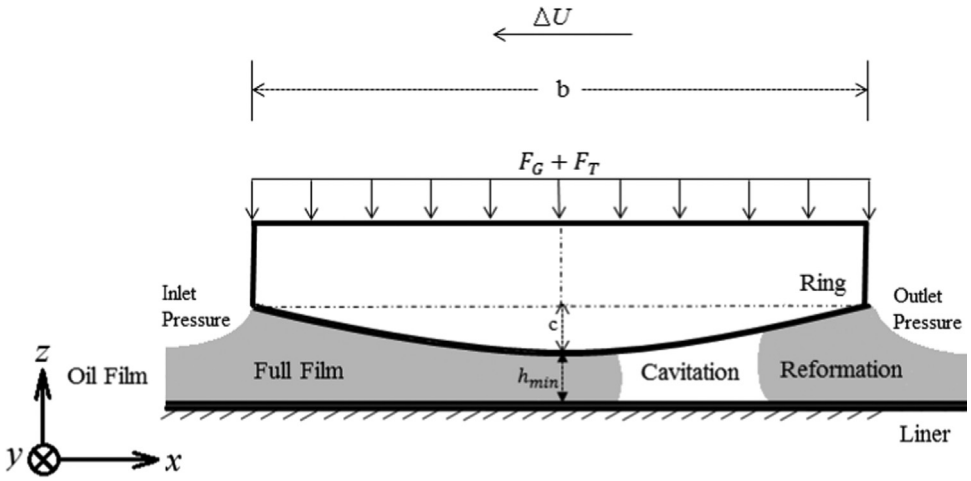

Fig. 1. Schematics of piston ring-liner conjunctional gap.

2. Physics of the problem

Fig. 1 shows the schematics of ring-liner conjunctional gap along the axial face-width of the ring. The ring subject to this analysis is a steel barrel faced rectangular ring[1], where the profile of the ring, $h_s(x)$ is assumed to be parabolic:

$$h_s(x) = \frac{cx^2}{(b/2)^2} \tag{1}$$

where, c is the crown height of the ring and b is its face-width.

In this paper good conformance of the ring to the liner surface is assumed in the circumferential direction of the bore. Therefore, the problem is simplified to a one dimensional contact, which is valid for ring-bore contact of bore diameter-to-ring face-width ratio: $2\pi r_0/b \geq 30$ as shown by Haddad and Tian [20], which is applicable to the engine studied here. The studied engine is a high performance V12 4-stroke naturally aspirated engine. The general data for the studied engine is provided in Table 1.

It is assumed that the ring does not undergo any relative motion with respect to the retaining groove. In practice, the ring may be subject to axial motion termed as ring flutter [5]. The piston sliding velocity is [21]:

$$\Delta U(\varphi) = -r\omega \sin\phi\left\{1 + \cos\varphi\left[\left(\frac{l}{r}\right)^2 - \sin^2\varphi\right]^{-\frac{1}{2}}\right\} \tag{2}$$

where φ is the crank-angle, l is the connecting rod length, r the crank pin radius and ω is the engine rotational speed. $\Delta U = U_2 - U_1 = U_2$ is the sliding velocity of the ring relative to the stationary liner: $U_1 = 0$.

The forces acting on the ring are considered as those in its radial plane. The ring is subjected to two outward forces: ring elastic tension force F_T and the gas forceF_G, acting on the inner rim of the ring. These forces conform the ring to the bore surface. Therefore, total outward force (towards the liner interface), acting on the ring is:

$$F = F_T + F_G \tag{3}$$

The ring tension force, F_T, is obtained as [22]:

$$F_T = p_e b r_0 \quad \left(\text{where } p_e = \frac{gEI}{3\pi b r_0^4}\right) \tag{4}$$

where, p_e is the elastic pressure, r_0 is the bore nominal radius and g is the ring end gap in its free (unfitted) state. The gas force acting on the back of the ring varies according to the chamber pressure in an engine cycle, thus:

$$F_G(\varphi) = 2\pi b r_0 p_g(\varphi) \tag{5}$$

The value of the gas pressure can be obtained through an appropriate blow-by analysis. In the current analysis the gas pressure is assumed to be equal to the in-cylinder pressure.

The outward radial forces (*i.e.* ring elastic tension and the gas force) are supported by the hydrodynamic reaction and the share of load carried by any interacting asperities. This is often the load shared by a small portion of asperities on the opposing surfaces. Thus, the instantaneous contact load is determined as $W(\varphi) = W_a(\varphi) + W_h(\varphi)$, where the hydrodynamic reaction is the integrated lubricant pressure distribution as follows:

$$W_h(\phi) = 2\pi r_0 \int_0^b p_h(\phi) dx\, dy \tag{6}$$

As shown in Fig. 1, in general, there are three conjunctions regions: (i) full film, (ii) film rupture and cavitation, and (iii) lubricant film reformation. A suitable two-phase flow model needs to be employed alongside the Navier–Stokes equations. This should take the form of vapour transport equation.

The share of load carried by the interacting asperities on the contiguous solid surfaces is obtained as [23]:

$$W_a = \frac{16\sqrt{2}}{15}\pi(\zeta\kappa\sigma)^2\sqrt{\frac{\sigma}{\kappa}}E^* A F_{5/2}(\lambda) \tag{7}$$

The dimensionless group $\zeta\kappa\sigma$ is known as the Tabor's roughness parameter, whilst σ/κ is a measure of a typical asperity slope [1]. These can be obtained through topographical measurements. E^* is the composite effective modulus of elasticity:

$$\frac{1}{E^*} = \frac{1-\nu_1^2}{E_1} + \frac{1-\nu_2^2}{E_2} \tag{8}$$

where ν_1 and ν_2 are the Poisson's ratios, and E_1 and E_2 the moduli of elasticity for the materials of bounding solid surfaces. The statistical function $F_{5/2}(\lambda)$ is introduced to match the assumed Gaussian distribution of asperities as a function of the Stribeck oil film parameter, $\lambda = h/\sigma$. Using a fifth-order polynomial curve fit this statistical function can be described as follows:

$$F_{5/2}(\lambda) = -0.0046\lambda^5 + 0.0574\lambda^4 - 0.2958\lambda^3 + 0.7844\lambda^2 - 1.0776\lambda + 0.6167 \tag{9}$$

[1] Internal combustion engines – Piston rings – Part 2: Rectangular rings made of steel should comply withISO 6622-2:2003

Table 1
Engine data.

Parameters	Values	Units
Crank-pin radius, r	39.75	mm
Connecting rod length, l	138.1	mm
Bore radius, r_0	44.5	mm
Ring crown height, c	10	μm
Ring axial face-width, b	1.15	mm
Ring radial width, d	3.5	mm
Ring free gap, g	10.5	mm

Table 2
Material properties and surface topographical parameters.

Parameters	Values	Units
Liner material	Grey cast iron[a]	–
Modulus elasticity of liner material	92.3	GPa
Poisson ratio for liner material	0.211	–
Density for liner material	7200	kg/m^3
Ring material	Steel SAE 9254[b]	–
Modulus elasticity of ring material	203	GPa
Poisson ratio for ring material	0.3	–
Roughness parameter ($\zeta\kappa\sigma$)	0.04	–
Measure of asperity gradient (σ/κ)	0.001	–
Density for ring material	7700	kg/m^3

[a] Centrifugal cast iron to ASTM-A 48, Class 30/DIN 1691 GG 30 standard.
[b] The ring has face coating of Chromium. The coating and slight back chamfer have known effects on ring tension and force correction factors, not taken into account in the current analysis. Back chamfers have a subtle, but important effect on the gas sealing of the ring against the groove.

Table 2 lists the materials' properties as well as the surface topographical parameters for both the compression ring and the cylinder liner.

3. Numerical model

3.1. General Navier–Stokes equation

The continuity and Navier–Stokes momentum equations for compressible viscous fluid flow are [24] as follows:

$$\frac{D\rho}{Dt}+\rho\nabla.\vec{V}=0 \tag{10}$$

$$\rho\frac{D\vec{V}}{Dt}=-\nabla p+\nabla.(\bar{\tau}_{ij})+\vec{F} \tag{11}$$

where D/Dt is the covariant derivative operator, ρ is the lubricant density, p is pressure, $\bar{\tau}_{ij}$ is the viscous stress tensor and $\vec{F}$ is the body force field vector. $\vec{V}=U\hat{i}+V\hat{j}+W\hat{k}$ is the velocity vector in which U is the component of velocity in the direction of axial lubricant entrainment, V is that in the side-leakage direction; along the y-axis (which may reasonably be discarded as there is negligible side-leakage in the thin film ring-bore conjunctional gap), and W is that in the direction of lubricant thickness. The viscous stress tensor is as follows:

$$\bar{\tau}_{ij}=\eta\left(\frac{\partial U_i}{\partial x_j}+\frac{\partial U_j}{\partial x_i}-\delta_{ij}\frac{2}{3}\nabla.\vec{V}\right) \tag{12}$$

where η is the local lubricant dynamic viscosity and δ_{ij} is the Kronecher delta. One possibility in a CFD model is to evaluate fluid viscosity as a function of pressure along the liner and into the depth of the lubricant film. The latter is neglected in the conventional hydrodynamic lubrication approach using Reynolds equation, where: $p/z=0$.

3.2. Cavitation model – vapour mass fraction and vapour transport equations

With cavitation, the liquid–vapour mass transfer (evaporation and condensation) is governed by the vapour transport equation as [25]:

$$\frac{\partial}{\partial t}(\alpha_v\rho_v)+\nabla.(\alpha_v\rho_v\vec{V}_v)=R_e-R_c \tag{13}$$

where ρ_v is the vapour density, $\vec{V}_v$ is the velocity vector of the vapour phase, R_e and R_c are mass transfer source terms related to the growth and collapse of vapour bubbles. The growth and collapse of a bubble cluster is modelled based on the Rayleigh–Plesset equation, describing the growth of a single vapour bubble in a liquid. This provides the rate equation, controlling vapour generation and condensation. Singhal et al. [26] assumed that a working fluid is a mixture of liquid and vapour and introduced a modified form of the above equation, based upon the vapour mass fraction, f_{mass} as follows:

$$\frac{\partial}{\partial t}(\rho_m f_{mass})+\nabla.(\rho_m\vec{V}_v f_{mass})=\nabla.(\Gamma\nabla f_{mass})+R_e-R_c \tag{14}$$

where ρ_m is the mixture density and Γ is the diffusion coefficient. The mass transfer rate expressions are derived from the Rayleigh–Plesset equations. The cavitation bubble size should be confined for the diminutive tribological conjunctions. This is based upon the limiting bubble size considerations (*i.e.* interfacial surface area per unit volume of vapour). The rates for formation/growth and collapse of cavitation bubbles are functions of the instantaneous local pressure and are given by:

$$R_e=C_e\frac{V_{ch}}{\sigma_s}\rho_l\rho_v\sqrt{\frac{2(p_{sat}-p)}{3\rho_l}}(1-f_{mass}),\quad \text{for}\quad p<p_{sat} \tag{15}$$

$$R_c=C_c\frac{V_{ch}}{\sigma_s}\rho_l\rho_v\sqrt{\frac{2(p-p_{sat})}{3\rho_l}}f_{mass},\quad \text{for}\quad p>p_{sat} \tag{16}$$

where the suffices l and v denote the liquid and vapour phases respectively, V_{ch} is the characteristic velocity, σ_s is the surface tension coefficient of the lubricant, p_{sat} is the liquid saturation vaporisation pressure at a given temperature and C_e and C_c are empirical constants, considered to be 0.02 and 0.01 respectively [26].

3.3. Lubricant rheology

The lubricant bulk rheological properties including density and viscosity are affected by pressure. The density–pressure relationship is [27]

$$\rho=\rho_0\left[1+\frac{0.6\times10^{-9}(p-p_{atm})}{1+1.7\times10^{-9}(p-p_{atm})}\right]\left[1-0.65\times10^{-3}(T-T_0)\right] \tag{17}$$

Using an analytical control volume thermal mixing model Morris et al. [28] showed that the lubricant temperature in the compression ring-liner conjunctional gap closely follows that of the

Table 3
Lubricant properties in atmospheric pressure and 40 °C.

Parameters	Values	Units
Lubricant viscosity, η_0	0.05	Pa s
Lubricant density, ρ_0	833	kg/m^3
α_0	1×10^{-8}	Pa^{-1}
β_0	0.004	K^{-1}
Atmospheric limiting shear stress (τ_{L0})	2.3	MPa
Pressure-induced shear coefficient (λ')	0.047	-
Average liner temperature for fired engine condition, T	160	°C

cylinder liner, with generated heat due to viscous shear heating of the lubricant in passage through the contact only accounting for less than 2%. Therefore, in the current analysis the average temperature of the liner, T is used (see Table 3). This temperature was measured directly from a fired engine. T_0 is considered to be the bulk oil sump temperature. Hence, no solution of energy equation was deemed necessary.

In the current analysis the measured average temperature of the lubricant (grade 5W30) is used for the vaporisation pressure. In practice the vaporisation pressure alters with lubricant temperature which in turn varies with the liner temperature as noted above.

The lubricant viscosity–pressure and temperature dependence is given as follows [29]:

$$\eta = \eta_0 \exp\{(\ln \eta_0 + 9.67) \times \left[-1 + \left(1 + 5.1 \times 10^{-9}(p - p_{atm})\right)^{z_0} \left(\frac{T - 138}{T_0 - 138}\right)^{-s_0}\right]\} \quad (18)$$

where

$$z_0 = \frac{\alpha_0}{5.1 \times 10^{-9}(\ln \eta_0 + 9.67)} \text{ and } s_0 = \frac{\beta_0 (T_0 - 138)}{(\ln \eta_0 + 9.67)} \quad (19)$$

where α_0 is the viscosity–pressure coefficient and β_0 is the viscosity–temperature coefficient. Details of lubricant rheological parameters are given in Table 3.

3.4. Boundary conditions

Fig. 2 shows the computation domain with the boundary surfaces being that of the ring and the liner. The boundary conditions are also indicated in the figure. The ring surface is subject to the sliding velocity U_2, whilst that of the liner is stationary. Furthermore, it is assumed that the lubricant adheres to the boundary solid surfaces (*i.e.* no slip boundary condition).

As it can be seen the pressure inlet and outlet boundary conditions are used for the lower and upper edges of the ring/liner contact as follows:

$$\begin{cases} p_h(-b/2) = p_L \\ p_h(+b/2) = p_U \\ p_h(x_c) = p_{sat} \end{cases} \quad (20)$$

Therefore, when the piston undergoes its upstroke motion, the inlet pressure is that of the combustion chamber shown in Fig. 3, whilst at the exit the crank-case pressure is assumed to be the atmospheric pressure. On the other hand, for the down-stroke sense of the piston, the inlet pressure is set to that of the crank-case (atmospheric) pressure, whilst the outlet pressure is that of the combustion chamber. The chamber pressure varies with the engine stroke, speed and throttle demand. Fig. 3 shows the measured in-cylinder pressure by a plug-type Kistler pressure transducer for the engine speed of 1500 rpm at 63% throttle input.

The cylinder liner has been assumed as the stationary wall with no-slip boundary condition. On the other hand, the ring is assumed as the moving wall with no-slip boundary condition. The engine sump (operation pressure) and cavitation vaporisation pressure are assumed to be at atmospheric pressure (101.3 kPa) at all times. No exit boundary condition such as the Swift–Steiber or Prandtl–Hopkins boundary conditions need to be stated with the Navier–Stokes approach.

3.5. Solution procedure

A 2D CFD model is developed. A computational mesh is generated using the ANSYS Design Modeller. The geometrical nature of the problem examined here imposes the use of only quadrilateral cells. After conducting a grid sensitivity analysis, 40 divisions were employed across the lubricant film (z-direction) and 1500 divisions along the ring face-width (x-direction), thus a mesh of 60,000 computational cells is used. Calculation of Reynolds number for the studied conditions showed that the flow is well within the laminar region.

A pressure-based mixture multi-phase model [30] is chosen for the present CFD analysis. No discrete regional control volume(s) of vapour are defined in such a model, which would require specifically defined boundary conditions. Instead, the mixture model provides the void fraction in various regions of the contact. The velocity–pressure coupling is treated using the SIMPLE algorithm and the second-order upwind scheme is employed for conservation of momentum to reduce the discretisation-induced errors in the calculation process. To achieve better accuracy, an error tolerance value of 10^{-6} is used for all the parametric residual terms.

Once the pressure distribution is obtained from the solution of Navier–Stokes equations, it is integrated over the contact area to obtain the hydrodynamic reaction (Eq. (6)).

The following solution procedure is followed:

Step 1: At a given crank angle, φ the total contact load F, exerted on the ring due to combustion gas pressure and ring elastic force is calculated (Eq. (3)).

Step 2: Assuming an initial value for the minimum film thickness (gap size), the lubricant pressure distribution and its rheological properties are calculated. The contact pressure

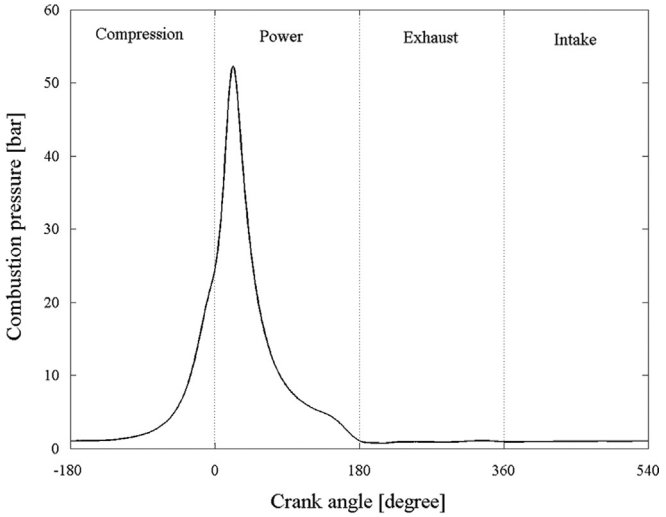

Fig. 3. Variation of chamber pressure with crank angle for engine speeds of 1500 rpm.

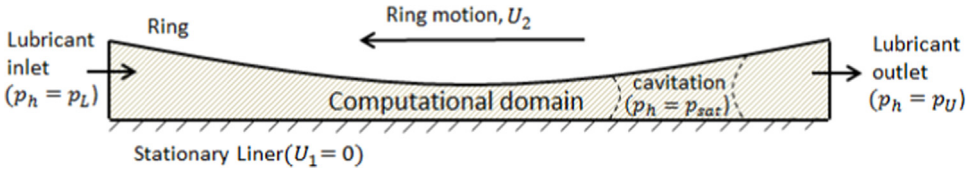

Fig. 2. Schematics of the computational domain and boundary conditions.

distribution is obtained using two-phase flow CFD analysis. It is noted that in the CFD approach the lubricant rheological properties are updated internally for the generated pressure and the assumed average contact temperature as the solution proceeds.

Step 3: The load carried by the asperities is calculated using Eq. (7). The pressure distribution is used to obtain the hydrodynamic reaction (Eq. (6)). Since the method of solution is quasi-static, this conjunctional reaction together with the asperity- carried load are assumed to support the total applied load exerted by the gas pressure and ring elastic force at each crank angle. The quasi-static balance of applied forces on the ring is sought through:

$$Err_{load}=\frac{|F(\varphi)-W(\varphi)|}{F(\varphi)}\leq 10^{-3} \tag{21}$$

If this criterion is not met, then the minimum film thickness is updated using the following equation:

$$h_m^n=(1+\delta X)h_m^o \tag{22}$$

where X is an adjusting parameter, $X=F(\varphi)-W(\varphi)/\max\{F(\varphi), W(\varphi)\}$. Superscripts n and o denote new and old steps in the iteration process. A damping coefficient $\delta=0.05$ is used to achieve faster load convergence, whilst maintaining numerical stability. It is noted that the 'dynamic mesh' concept [31] is employed for variations in the minimum film thickness in the CFD analysis. A smoothing mesh method is used with a convergence tolerance of 10^{-5}.

With a new value for the minimum film thickness, the Steps 2 to 3 are repeated until the convergence criterion in Step 3 is met.

4. Analytically determined boundary conditions

Tipei [17] investigated the inlet and outlet boundaries of the domain in hydrodynamic contacts. He noted that in the inlet zone, there are swirl flows, where some reverse flow (counter flow) occurs at the inlet as is also observed in the experimental observations [32]. This means that only a fraction of the lubricant at the inlet meniscus is admitted into the contact domain. The counter flows cease at the stagnation point, where: $\partial\vec{V}/\partial z=0$ and $\vec{V}=0$ (is the normal direction to the conjunction plane). This condition os known as the Prandtl–Hopkins boundary condition and defines the zero-reverse flow boundary. Considering the potential flows in the inlet region, Tipei found the compatibility condition as follows [17]:

$$\begin{aligned}&\cot^2\pi\left[\tfrac{1}{2}-\tfrac{1-k}{f(k)}\right]-\cot^2\pi\sqrt{\left[\tfrac{1}{2}-\tfrac{1-k}{f(k)}\right]^2-\tfrac{2k}{f(k)}}\\&=\cot\pi\left\{\frac{1}{2}-\frac{1-k}{f(k)}-\sqrt{\left[\frac{1}{2}-\frac{1-k}{f(k)}\right]^2-\frac{2k}{f(k)}}\right\}\\&\times\cot\pi\left\{\frac{1}{2}-\frac{1-k}{f(k)}+\sqrt{\left[\frac{1}{2}-\frac{1-k}{f(k)}\right]^2-\frac{2k}{f(k)}}\right\}\end{aligned} \tag{23}$$

where

$$k=\frac{U_1}{U_2} \tag{24}$$

where U_1 and U_2 are surface velocities of contacting bodies (cylinder liner and the piston ring respectively). The function $f(k)$ depends on the pressure gradient at the inlet. The values of $f(k)$ for the usually encountered cases of the surface velocity ratio k are listed in Table 4. In the case of the piston ring conjunctional gap, $k=0$ and $f(k)=4$.

Table 4
Calculated values for $f(k)$.

k	$f(k)$
0	4
0.5	7.8
1	32/3

Tipei [17] assumed a similar approach for the determination of separation boundary at the exit constriction, leading to the determination of the lubricant film rupture point, using the Prandtl–Hopkins conditions:

$$\frac{\cosh\vartheta_i}{\cosh\vartheta_e}=\frac{1-\frac{1}{3}(1+\frac{2\sqrt{k}}{1+k})}{1-\frac{f(k)}{6(1+k)}} \tag{25}$$

$$\begin{aligned}&\left[1-\tfrac{1}{3}\left(1+\tfrac{2\sqrt{k}}{1+k}\right)\right]\tanh\vartheta_e-\left[1+\tfrac{f(k)}{6(1+k)}\right]\tanh\vartheta_i-\left[1-\tfrac{f(k)}{6(1+k)}\right]\\&\cosh\vartheta_i\left[\arcsin(\tanh\vartheta_e)-\arcsin(\tanh\vartheta_i)\right]=0\end{aligned} \tag{26}$$

ϑ_i and ϑ_e are the ratios of film thickness at the inlet and the exit to the minimum film thickness respectively. Therefore, after calculating the parameters from Eqs. (25) and (26) and having the minimum film thickness and the film shape (Eq. (1)), the distance of the inlet stagnation and outlet separation points from the centre of the ring can be found. This assumption agrees well with the experimental observations of Birkhoff and Hays [32] and Mohammadpour et al. [16].

Alternatively if instead of the Prandtl–Hopkins boundary condition the Swift–Stieber conditions ($\partial p/\partial z=0$ and $p=0$) is used, then:

$$\frac{\cosh\vartheta_e}{\cosh\vartheta_i}=1-\frac{f(k)}{6(1+k)} \tag{27}$$

and

$$\begin{aligned}&\tanh\vartheta_e-\left[1+\tfrac{f(k)}{6(1+k)}\right]\tanh\vartheta_i-\left[1-\tfrac{f(k)}{6(1+k)}\right]\cosh\vartheta_i\\&\times\left[\arcsin(\tanh\vartheta_e)-\arcsin(\tanh\vartheta_i)\right]=0\end{aligned} \tag{28}$$

These two boundary conditions give similar values at the inlet, but predict different values for the lubricant film rupture points at the outlet. Later, it is shown that the Prandtl–Hopkins boundary conditions conform closer to the open exit boundary determined through two-phase flow solution of Navier–Stokes equations.

5. Determination of generated friction

A friction model is required in order to calculate the parasitic losses in the conjunction. The total friction comprises two components; boundary friction and viscous friction:

$$f_t=f_v+f_b \tag{29}$$

At any instant of time, viscous shear of the lubricant film is obtained as [1]:

$$\vec{\tau}=\left|\pm\frac{h}{2}\nabla p-\Delta\vec{V}\frac{\eta}{h}\right| \tag{30}$$

If the shear stress remains below the limiting shear stress of the lubricant [33,34], then the calculated value from Eq. (30) is used. For shear values exceeding the limiting value, which is a property of lubricant and dependent on pressure, the limiting shear stress becomes [34]:

$$\tau_L=\tau_{L0}+\lambda' p \tag{31}$$

The values of the coefficients in the above equation are presented in Table 3. Then, the viscous friction force is obtained as:

$$f_v = \tau A, \tag{32}$$

where $A = 2\pi r_0 b$ is the apparent contact area.

When the Stribeck oil film parameter, $\lambda = h/\sigma \leq 3$, a mixed regime of lubrication is encountered. In this case a non-Newtonian high shear thin film is assumed to form at the summit of the asperities or trapped in-between them. Under this condition, the shear stress can exceed its limiting value, and it is assumed to equate to the limiting value given by Eq. (31). The asperity pressure is as follows:

$$p_a = \frac{W_a}{A_a} \tag{33}$$

The share of load carried by the asperities, W_a is calculated using Eq. (7). A small portion of asperities carry this load, the total summit area of which is obtained through statistical analysis. For an assumed Gaussian distribution of asperities, this area is obtained as follows [23]:

$$A_a = \pi^2(\zeta\kappa\sigma)^2\sqrt{\frac{\sigma}{\kappa}}AF_2(\lambda) \tag{34}$$

where $F_2(\lambda)$ is a function, representative of the Gaussian distribution of asperities in terms of λ (the Stribeck oil film parameter):

$$F_2(\lambda) = -0.0018\lambda^5 + 0.0281\lambda^4 - 0.1728\lambda^3 + 0.5258\lambda^2 - 0.8043\lambda + 0.5003 \tag{35}$$

Now having the limiting shear stress at the asperity tips and the asperity surface area, the boundary friction can be calculated as follows:

$$f_b = \tau_L A_a \tag{36}$$

Therefore, the combination of Eqs. (29)–(36) and Eq. (7) gives the total friction generated in the conjunctional gap. The total power loss from the ring-bore conjunctional gap is due to this friction:

$$P_f = f\Delta U \tag{37}$$

6. Results and discussion

Initially, a comparison is made between the inlet and outlet boundaries predicted through the current CFD approach and those calculated using the analytical method (described in Section 4) using the approach highlighted originally by Tipei [17]. The potential flow analysis (Eqs. (23) and (24)), together with the Prandtl–Hopkins boundary conditions yield one set of inlet and outlet conditions. Alternatively, the solution of the same potential flow with Swift–Stieber boundary conditions results in another set of inlet and outlet conditions. The intention for this comparative study is twofold. Firstly, it constitutes a form of validation for the CFD approach as the analytical approach has shown very good agreement for the determination of boundary conditions with the experimental observations of Birkhoff and Hays [32] as well as with the experimental circular point contact conditions [18], both under rolling conditions. Secondly, the applicability of the analytical method for the determination of boundary conditions for sliding contacts can also be ascertained.

Table 5 lists 3 sets of predicted inlet and outlet boundaries, 2 of which are based on the analytical method for Prandtl–Hopkins and Swift–Stieber boundary conditions respectively (using the potential flow analysis) and the third set is that obtained by the current CFD approach. Close agreement between the CFD predictions and the analytical results can be observed. CFD – predicted inlet stagnation boundary agrees very well with both the Swift–Stieber and Prandtl–Hopkins boundary conditions. For the outlet boundary conditions, the CFD results conform much closer to the Swift–Stieber boundary.

Table 5
Calculated inlet and outlet distances (stagnation point and separation point).

	CFD	Analytical method, Prandtl–Hopkins boundary condition	Analytical method, Swift–Stieber boundary condition
Inlet distance [μm]	267	265	260
Outlet distance [μm]	85	151	76

In fact, most reported analyses of piston ring conjunctional gap routinely employ the Swift–Stieber boundary conditions at the exit constriction [9–11,35,36]. Arcoumanis et al. [37] reported numerical analysis of compression ring conjunctional gap with various outlet boundary conditions, including Swift–Stieber, limiting case of the Floberg boundary and the Coyne–Elrod cavitation boundary [38]. They found that the predicted film thickness, using the Swift–Stieber boundary conditions showed closer agreement with their experimentally measured film thickness. Their findings are in line with the current CFD predictions and the analytical potential flow analysis described here.

Fig. 4 is a typical velocity flow field for the inlet-to-central conjunctional region, obtained through the current analysis. It shows the stagnation point, where the zero-reverse inlet boundary is reached ($\partial\vec{V}/\partial z = 0$ and $\vec{V} = 0$), Prandtl–Hopkins inlet boundary. This point is far from the usually assumed fully flooded inlet, which is often assumed to be at the leading edge of the ring, beyond the swirl flow region. This finding indicates that only a portion of an assumed available flow is admitted into the conjunction-proper beyond the stagnation point. Hence, under the conditions shown, and in fact throughout the engine cycle, only a partially flooded inlet is attained. The reason for this is the recirculating (swirl) flow in the inlet wedge of the conjunction as shown clearly in the zoomed-in inset to the figure.

The recirculating flow is a function of the velocity ratio of the contiguous surfaces which alters according to the piston sliding velocity. This is a function of the crank angle position. It also depends on the wedge angle as a function of the ring profile, which in turn determines the minimum film thickness. Therefore, load carrying capacity of the conjunctional gap is affected by the ring profile and the inlet boundary (the inlet wedge velocity flow field). As the hydrodynamic load carrying capacity is critical in guarding against asperity interactions, in theory, one can optimise the ring contacting face-width to enhance the load carrying capacity.

Fig. 5 shows the generated conjunctional pressure distributions for the actual ring face-width of $b = 1.15$ mm (Table 1) and its variously assumed multiples up to $3b$ in the down-stroke sense of the piston. The leading edge of the ring is at the assumed atmospheric pressure (gauge pressure, $p = 0$ in the figure). A minimum film thickness of 1μm is assumed (as a constraint) in this analysis. This enables the study of load carrying capacity of the contact as influenced by the changes arising at the inlet with differing ring face-widths.

As expected, the results show increasing load carrying capacity because of an increased conjunctional area. However, the increase is not proportional to the contact face-width as would be the case with an assumed fully flooded inlet, where:

$$W_h = \frac{2.9b\eta\Delta U}{h_0} \tag{38}$$

which is based on the Swift–Stieber exit boundary condition [1], h_0 being the minimum film thickness (kept constant for all the cases in Fig. 5). Hence, at the same ring sliding speed, ΔU, $W_h \propto b$, Thus, doubling the ring face-width would double the load carrying

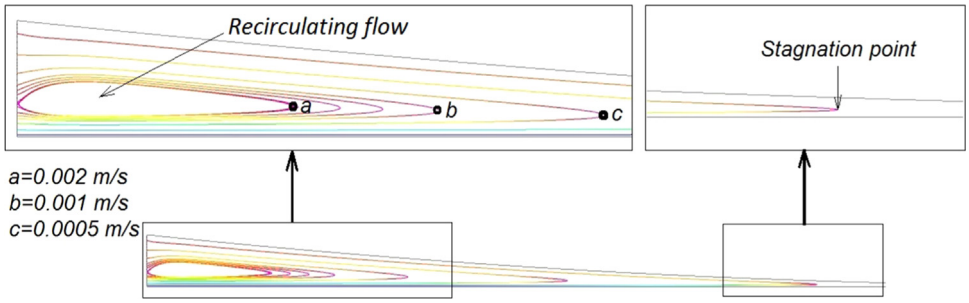

Fig. 4. Typical velocity flow field in the inlet region of the sliding conjunction.

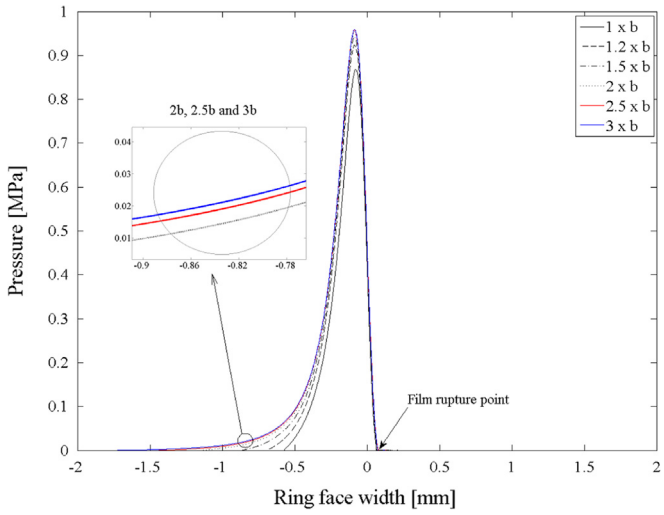

Fig. 5. The streamlines of the flow in the ring specified in Table 2 compared with those of various scaled widths.

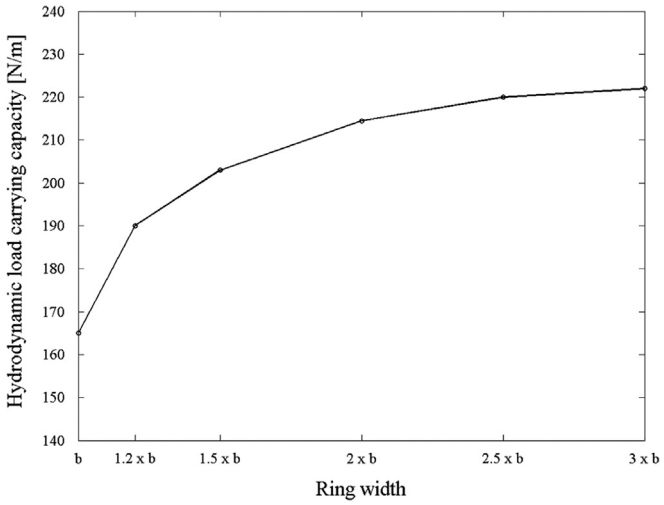

Fig. 6. Shows the load carrying capacity per unit length for different rings of Fig. 5.

capacity. With realistic boundary conditions the position of the stagnation point alters and thus the area of conjunction-proper is not a direct function of ring face-width only. Therefore, the load carrying capacity and the pressure distribution are dependent on the inlet flow field. The results in Fig. 5 show that the inlet trail to the position $p=0$ on the left-hand side of the pressure traces is extended with an increasing face-width, but in none of the cases reaches anywhere near the leading edge of the ring (*i.e.* all contacts are only partially flooded). Furthermore, progressively increasing the ring face-width only marginally lengthens the conjunctional inlet trail as shown in the inset to the figure. Thus, progressively a reduced load carrying capacity would result. Fig. 6 clearly shows this trend. The underlying reason is best observed by the inward flow into the contact conjunction. This is shown in Table 6. The physical inlet is assumed at the leading edge of the ring face-width. This is analogous to assuming a fully flooded inlet. Clearly, if a constant minimum film thickness is assumed at the same sliding velocity, but with an increased contact area, then a larger volumetric lubricant flow rate is required to maintain fully flooded conditions. The difference in the flow rate at the physical inlet and that at the central contact through the minimum film thickness accounts for the backward (reverse and swirl) flow in the inlet zone. It can be seen that this difference progressively increases with an increasing ring face-width. Therefore, only a portion of the volume of the lubricant made available at the nib of the contact is actually admitted to the contact conjunction, and in none of the cases a fully flooded condition is noted. This is the reason behind partially flooded lubricated contacts in practice, which is not confined to the ring-liner conjunctional gap only. Clearly, the outward flow from the contact at the separation boundary equates that through the minimum film thickness constriction. This is simply a

Table 6
Mass flow rates through the content.

	Physical inlet flow (kg/s)	Central contact flow (kg/s)	Outlet flow(kg/s)
B	8.88×10^{-5}	8.751×10^{-5}	8.751×10^{-5}
1.2*b*	9.95×10^{-5}	8.792×10^{-5}	8.792×10^{-5}
1.5*b*	1.12×10^{-4}	8.825×10^{-5}	8.825×10^{-5}
2*b*	1.27×10^{-4}	8.848×10^{-5}	8.848×10^{-5}
2.5*b*	1.37×10^{-4}	8.858×10^{-5}	8.858×10^{-5}
3 *b*	1.40×10^{-4}	8.860×10^{-5}	8.860×10^{-5}

restatement of the principle of conservation of mass, embodied in continuity equation together with the Navier–Stokes equations. The flow at the outlet, beyond the lubricant film rupture boundary can contain significant vapour content, thus the reason for the inclusion of vapour transport equation in the analysis.

Often fully flooded inlet conditions are assumed during the various engine strokes. However, the measured friction [6–8] or film thickness [39] indicate mixed or boundary regimes of lubrication at or in the vicinity of the TDC. Hydrodynamic regime of lubrication is found to be dominant in other locations, such as at piston mid-span locations in the various engine strokes. Fig. 7 shows the predicted minimum film thickness at various locations. Mid-span locations are in the compression stroke (-90° crank angle), power stroke (90° crank angle), exhaust stroke (270° crank angle) and the intake stroke (450°crank angle). The positions $\pm5^\circ$ crank angle correspond to the transition from the compression to power stroke through the TDC, where mixed or boundary regimes of lubrication are prevalent [7–11]. Obviously, the minimum film thickness is reduced for all ring face-width cases during the reversal because of the reducing sliding velocity of the piston. The minimum

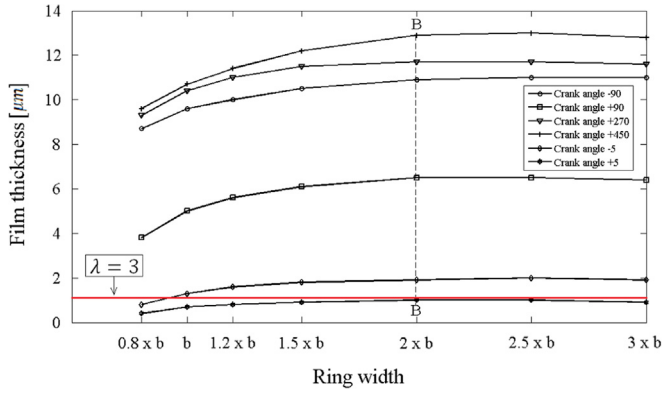

Fig. 7. Variation of minimum film thickness for different ring widths at piston mid-span positions and 5° crank angle either side of the TDC (combustion).

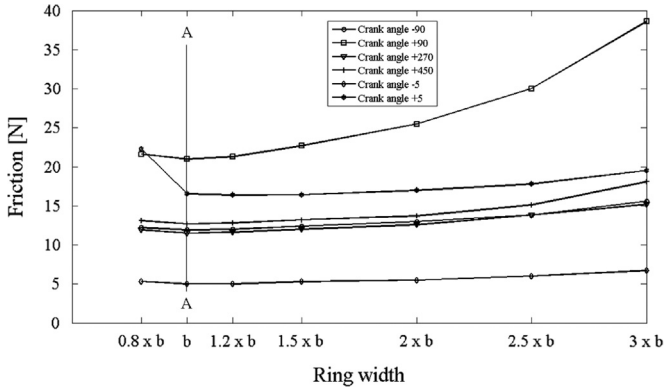

Fig. 8. Variation of friction for different ring widths for piston at mid-span positions.

film thickness is also reduced during the compression and power strokes, because of increased pressure loading behind the ring. The line = 3, where $=h/\sigma_{RMS}$ is the Stribeck's oil film parameter, represents the boundary between lubricated hydrodynamic condition and mixed regime of lubrication. It can be seen that for the region $-5^\circ \le \varphi \le 5^\circ$ the lubricant film thickness is quite thin and thus a mixed regime of lubrication would be expected.

It can be seen that in all cases the film thickness gradually increases up to the ring face-width of 2*b* before no further gain is noted. The contact load, *F* (Eq. (3)) is known for the ring-liner conjunction at these locations. Therefore, an increasing film thickness with the broadening ring contact face-width (up to an optimum) is indicative of enhanced hydrodynamic action. To ascertain this, it would be instructive to determine the total friction (viscous and boundary contributions) for these cases.

Fig. 8 shows the predicted friction for the same positions as in Fig. 7. There is no correspondence between the optimum conditions in Fig. 7 (thickest minimum conjunctional film for a ring face-width of 2*b*, indicated by the vertical line BB) and the minimum conjunctional friction for the ring width *b* (line AA in Fig. 8). In the piston mid-span locations there is insignificant contribution due to asperity interactions as the minimum lubricant film thickness is in excess of 3 μm in all cases (Fig. 7), the least film thickness of the investigated crank angles occurring during the power stroke (crank angle of 5°). Furthermore, the change in the film thickness is fairly small in the case of each particular location, thus changes in viscous shear (Eq. (30)) are marginal when dealing with a particular crank angle. Of course, these changes are not negligible at different crank angle positions, because of the sliding speed, effective lubricant viscosity and the

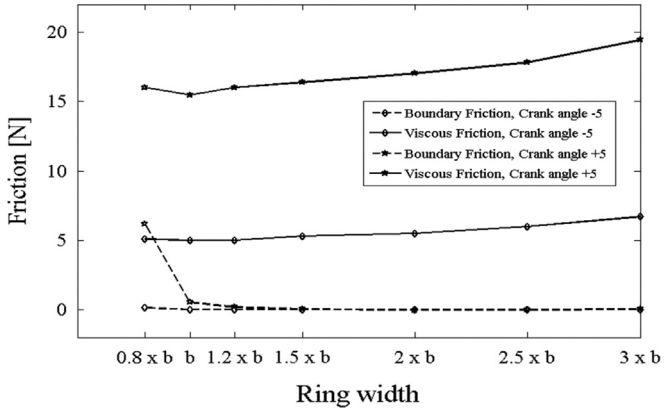

Fig. 9. Viscous and boundary contributions to generated friction immediately prior to, and just after the TDC reversal (combustion).

film thickness (see Eq. (38)). The increasing friction is also as the result of increased lubricated contact area between the inlet stagnation point (the zero reverse boundary) and the lubricant film rupture point. This indicates that maximum viscous friction occurs at the mid-span position in the power-stroke, whilst the maximum boundary friction takes place at the TDC reversal for the crank angle of 5°. In fact, Fig. 9 shows the contributions from viscous and boundary frictions during the TDC reversal. Even in these locations the main contribution is due to viscous friction, with fairly thin films and increased pressure loading behind the ring; Poiseuille friction. The shear stress is given by Eq. (30), where the first term on the right-hand side is the contribution due to Poiseuille shear, which is a function of pressure gradient, which is higher at the TDC reversal and increases in the power stroke.

Fig. 10 shows the position of lubricant film rupture and the subsequent cavitation region, which is also shown by the zoomed-in inset to the figure. The contours in the figure represent different levels of void fraction (volume fraction of liberated vapour in the bulk lubricant). The figure shows significant amount of vapour content, which reduces both the load carrying capacity as well as viscous friction.

Fig. 11 shows the variation in vapour fraction for various crank-angle positions with different assumed ring contacting face-width. Important points to note are reduced vapour fraction in the power stroke in comparison with that in the other strokes. This is expected, because of a higher contact pressure. This is clearly shown through the TDC reversal where there is lower vapour fraction for the crank angle of 5° (start of the power stroke) than −5° (end of the compression stroke). With less vapour content, viscous friction is increased accordingly (Figs. 7 and 8).

7. Conclusions

The paper shows that the compression ring-liner conjunctional gap is only partially flooded, irrespective of a sufficient volume of lubricant assumed at a physical inlet set at the leading edge of the ring. The inlet and outlet boundary conditions, determined through combined solution of Navier–Stokes and vapour transport equations, conform closely to the potential flow analysis of Tipei [17]. This puts the realistic inlet boundary at the stagnation point, where no reverse flow takes place. This is in line with the use of Prandtl–Hopkins boundary conditions. At the contact outlet, the current analysis agrees with Swift–Stieber boundary conditions to determine the position of lubricant film rupture. Furthermore, the use of Rayleigh–Plesset equation within the analysis determines the cavitation zone.

The key finding of the analysis is the determination of the effect of ring contact face to optimise tribological conditions. This shows that a unique optimal ring face-width cannot be found, which

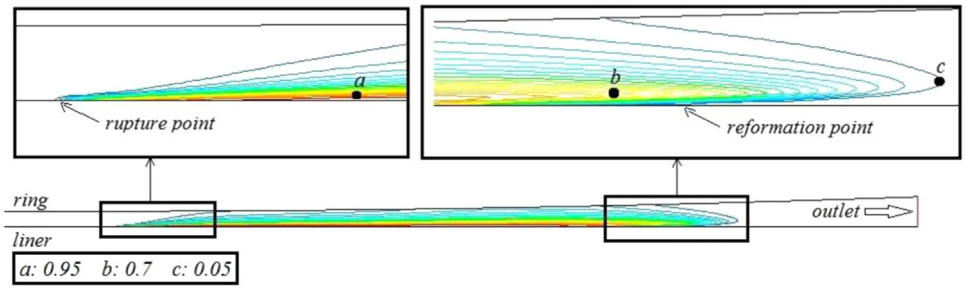

Fig. 10. Contact exit boundary with contours of vapour content.

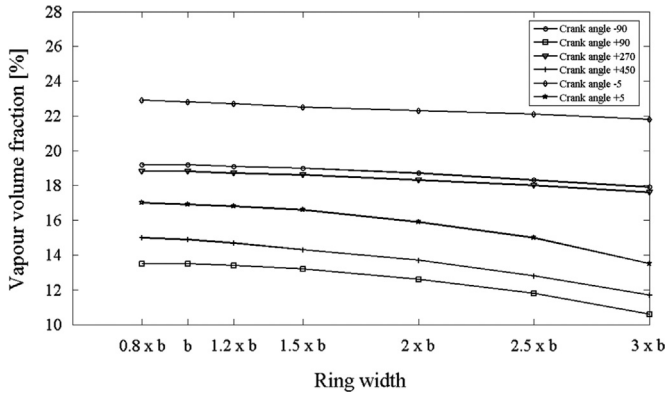

Fig. 11. Vapour content variation in different engine strokes and ring face-width.

would optimise film thickness (thus, the load carrying capacity) as well as friction (comprising viscous and boundary contributions). This is because of the transient nature of the conjunction, which is also affected by contact temperature, generation of vapour and changes in contact kinematics as well as gas pressure loading.

Ideally, a near-optimal solution can be sought through multivariate optimisation techniques. However, there are also practical engineering considerations which may inhibit use of certain ring geometries. At high speeds the ring is subject to high inertial forces, which would potentially, at critical points, unseat the more heavier compression rings (*e.g.* $>3b$) from their lower sealing face, thereby degrading operational performance [39]. Indeed, ISO 6622-2 suggests that ring widths should be limited to an upper limit of 2.5 mm (or 2.17*b* in the case of the current analysis). On the other hand, a thin ring (e.g. 0.8*b*) can be subject to considerable modal response (radial in-plane vibration and axial out-of-plane twist [3,4]), which can result in loss of sealing, blow-by and reverse blow-by.

Together with material and manufacturing limitations, the above considerations effectively narrows the available choice of ring axial face-width to a far narrower band than that implied by the results of parametric optimisation studies highlighted here.

Acknowledgements

The authors wish to express their gratitude to the Lloyd's Register Foundation (LRF) for the financial support extended to the International Institute for Cavitation Research. Thanks are also due to the Engineering and Physical Sciences Research Council (EPSRC) for the Encyclopaedic Programme Grant (EP/G012334/1); some of research findings of which are used in this paper. The technical and financial support of Capricorn Automotive is also acknowledged.

References

[1] Gohar R, Rahnejat H. Fundamentals of tribology. London, UK: Imperial College Press; 2008 ISBN: 10-1-84816-184-0.
[2] Richardson DE. Review of power cylinder friction for diesel engines. Trans ASME, J Tribol 2000;122(4):506–19.
[3] Baker CE, Theodossiades S, Rahnejat H, Fitzsimons B. Influence of in-plane dynamics of thin compression rings on friction in internal combustion engines. J Eng Gas Turbines Power 2012;134(9):092801.
[4] Tian T. Dynamic behaviours of piston rings and their practical impact; Part 1: ring flutter and ring collapse and their effects on gas flow and oil transport. Proc Inst Mech Eng, Part J: J Eng Tribol 2002;216:209–27.
[5] Rahmani R, Theodossiades S, Rahnejat H, Fitzsimons B. Transient elastohydrodynamic lubrication of rough new or worn piston compression ring conjunction with an out-of-round cylinder bore. Proc IMechE, Part J: J Eng Tribol 2012;226(4):284–305.
[6] Sherrington I. Measurement techniques for piston-ring tribology. Tribol Dyn Engine Powertrain: Fundam, Appl Future Trends 2010:387.
[7] Furuhama S, Sasaki S. New device for the measurement of piston frictional forces in small engines, SAE, Paper no. 831284; 1983.
[8] Gore M, Theaker M, Howell-Smith S, Rahnejat H, King PD. Direct measurement of piston friction of internal-combustion engines using the floating-liner principle. Proc IMechE, Part D: J Automob Eng 2014;228(3):344–54.
[9] Ma MT, Sherrington I, Smith EH. Implementation of an algorithm to model the starved lubrication of a piston ring a distorted bores: prediction of oil flow and onset of gas blow-by. Proc IMechE, Part J: J Eng Tribol 1996;210:29–44.
[10] Morris N, Rahmani R, Rahnejat H, King PD, Fitzsimons B. The influence of piston ring geometry and topography on friction. Proc IMechE, Part J: J Eng Tribol 2012;227(2):141–53.
[11] Chong WWF, Teodorescu M, Vaughan ND. Cavitation induced starvation for piston-ring/liner tribological conjunction. Tribol Int 2011;44(4):483–97.
[12] Elrod SHG. A cavitation algorithm. Trans ASME, J Lubr Technol 1981; 103(3):350–4.
[13] Jakobsson B, Floberg L. The finite journal bearing considering vaporisation. Gothenburg, Sweden: Trans. of Chalmers University of Tech; 1957.
[14] Olsson KO. "Cavitation in dynamically loaded bearings". Trans. of Chalmers University of Technology; 1965.
[15] Sahlin F, Almqvist A, Larsson R, Glavatskih S. A cavitation algorithm for arbitrary lubricant compressibility. Tribol Int 2007;40(8):1294–300.
[16] Shahmohamadi H, Rahmani R, Rahnejat H, Garner CP, King PD. Thermo-mixed hydrodynamics of piston compression ring conjunction. Tribol Lett 2013; 51(3):323–40.
[17] Tipei N. Boundary conditions of a viscous flow between surfaces with rolling and sliding motion. Trans ASME, J Lubr Technol 1968;90(1):8–16.
[18] Mohammadpour M, Johns-Rahnejat PM, Rahnejat H, Gohar R. Boundary conditions for elastohydrodynamics of circular point contacts. Tribol Lett 2014;53(1):51–70.
[19] Johns-Rahnejat PM, Gohar R. Measuring contact pressure distributions under elastohydrodynamic point contacts. Tribotest 1994;1(1):33–53.
[20] Haddad SD, Tian K-T. Analytical study of offset piston and crankshaft designs and the effect of oil film on piston slap excitation in a diesel engine. Mech Mach Theory 1995;30(2):271–84.
[21] Rahnejat H. Multi-body dynamics: vehicles, machines and mechanisms. Bury St Edmunds: Professional Engineering Publishing; 0768002699.
[22] Bin Chik A, Fessler H. Radial pressure exerted by piston rings. J Strain Anal Eng Des I 1966;2:165–71.
[23] Greenwood JA, Tripp JH. The contact of two nominally flat rough surfaces. Proc IMechE 1970–1971;185:625–34.
[24] White FM. Viscous fluid flow. 2nd EditionMcGraw-Hill; 1991.
[25] Senocak I, Shyy W. Interfacial dynamics-based modelling of turbulent cavitating Flows, Part-1: Model development and steady-state computations. Int J Numer Methods Fluids 2004;44:975–95.
[26] Singhal AK, Li HY, Athavale MM, Jiang Y. Mathematical basis and validation of the full cavitation model ASME FEDSM'01, New Orleans, Louisiana; 2001.
[27] Dowson D, Higginson GR. A numerical solution to elastohydrodynamic problem. J Mech Eng Sci 1959;1(1):6–15.
[28] Morris N, Rahmani R, Rahnejat H, King PD, Fitzsimons B. Tribology of piston compression ring conjunction under transient thermal mixed regime of lubrication. Tribol Int 2013;59:248–58.
[29] Houpert L. New results of traction force calculations in elastohydrodynamic contacts. Trans ASME, J Tribol, 107; 1985. p. 241–8.
[30] Manninen M, Taivassalo V, Kallio S. On the mixture model for multiphase flow/VTT publications 288 technical research centre of Finland; 1996.

[31] Snyder DO, Koutsavdis EK, Anttonen JSR. Transonic store separation using unstructured CFD with dynamic meshing. Technical Report AIAA-2003-3913, 33th AIAA Fluid Dynamics Conference and Exhibition, American Institute of Aeronautics and Astronautics; 2003.
[32] Birkhoff G, Hays D. Free boundaries in partial lubrication. J Math Phys 1963; 42(2):126–38.
[33] Briscoe BJ, Evans DCB. The shear properties of Langmuir–Blodgett layers. Proc RSoc, Ser A.: Math Phys Sci 1982;380(1779):389–407.
[34] Mohammadpour M, Theodossiades S, Rahnejat H, Saunders T. Non-Newtonian mixed elastohydrodynamics of differential hypoid gears at High Loads. Meccanica 2014;49(5):1115–38.
[35] Bolander NW, Steenwyk BD, Sadeghi F, Gerber GR. Lubrication regime transitions at the piston ring-cylinder liner interface. Proc IMechE. Part J: J EngTribol 2005;219:19–31.
[36] Mishra PC, Balakrishnan S, Rahnejat H. Tribology of compression ring-to-cylinder contact at reversal. Proc IMechE, Part J: J Eng Tribol 2008; 222(7):815–26.
[37] Arcoumanis, C, Duszynski, M, Flora, H, Ostovar, P, Development of a piston-ring lubrication test-rig and investigation of boundary conditions for modelling lubricant film properties. SAE Technical Paper 952468; 1995.
[38] Coyne JC, Elrod HG. “Conditions for the rupture of a lubricating fil—Part II: new boundary conditions for Reynolds equation. Trans ASME, J Tribol 1971;93 (1):156–67.
[39] Furuhama, S, Hiruma, M, Tsuzita, M. Piston ring motion and its influence on engine tribology. SAE Technical Paper790860, 1979.